Nanoscale

PAPER

View Article Online
View Journal | View Issue

Cite this: *Nanoscale*, 2024, **16**, 14366

Nanoscale core–shell structure and recrystallization of swift heavy ion tracks in $SrTiO_3$

Ashish Kumar Gupta, [a] Eva Zarkadoula, [b] Maxim Ziatdinov, [c] Sergei V. Kalinin, [d,e] Vikas Reddy Paduri, [a] Jordan A. Hachtel, [b] Yanwen Zhang, [f] Christina Trautmann,[g,h,i] William J. Weber *[e] and Ritesh Sachan *[a]

It is widely accepted that the interaction of swift heavy ions with many complex oxides is predominantly governed by the electronic energy loss that gives rise to nanoscale amorphous ion tracks along the penetration direction. The question of how electronic excitation and electron–phonon coupling affect the atomic system through defect production, recrystallization, and strain effects has not yet been fully clarified. To advance the knowledge of the atomic structure of ion tracks, we irradiated single crystalline $SrTiO_3$ with 629 MeV Xe ions and performed comprehensive electron microscopy investigations complemented by molecular dynamics simulations. This study shows discontinuous ion-track formation along the ion penetration path, comprising an amorphous core and a surrounding few monolayer thick shell of strained/defective crystalline $SrTiO_3$. Using machine-learning-aided analysis of atomic-scale images, we demonstrate the presence of 4–8% strain in the disordered region interfacing with the amorphous core in the initially formed ion tracks. Under constant exposure of the electron beam during imaging, the amorphous part of the ion tracks readily recrystallizes radially inwards from the crystalline-amorphous interface under the constant electron-beam irradiation during the imaging. Cation strain in the amorphous region is observed to be significantly recovered, while the oxygen sublattice remains strained even under the electron irradiation due to the present oxygen vacancies. The molecular dynamics simulations support this observation and suggest that local transient heating and annealing facilitate recrystallization process of the amorphous phase and drive Sr and Ti sublattices to rearrange. In contrast, the annealing of O atoms is difficult, thus leaving a remnant of oxygen vacancies and strain even after recrystallization. This work provides insights for creating and transforming novel interfaces and nanostructures for future functional applications.

Received 7th May 2024,
Accepted 28th June 2024

DOI: 10.1039/d4nr01974a

rsc.li/nanoscale

Introduction

It is well-established that atomic rearrangements caused by ion-solid interactions result in the production of defects and phase transformations and thus introduce new functional properties or modify their conventional behavior of complex oxides. Several examples of ion-beam modifications not naturally present in complex oxides have been reported. For example, forming oxygen vacancy defects gives rise to blue-light emission,[1] metastable ferroelectricity,[2] and localized conductivity[3] in perovskite-structured $SrTiO_3$. Similarly, metallic-to-insulator and ferromagnetic-to-antiferromagnetic transitions can be achieved in $La_{0.7}Sr_{0.3}MnO_3$ thin films *via* controlling the vacancy defect concentration profile through He ion irradiation.[4] Various studies have been reported the fundamental discoveries on the effect on cationic radii and the local environment around the cations that lead to an order–disorder phase transformation. It has been seen that the tendency of phase transformation in pyrochlore structure oxides ($A_2B_2O_7$) from amorphous to disordered defect-fluorite phase grows with increasing size of the B-site cation (Ti to Zr).[5,6] The local disorders at the atomic sites leading to the formation of new metastable phases, such as weberite and defect-fluorite, have

[a]*School of Mechanical and Aerospace Engineering, Oklahoma State University, Stillwater, OK 74078, USA. E-mail: rsachan@okstate.edu*
[b]*Center for Nanophase Materials Sciences, Oak Ridge National Laboratory, Oak Ridge, TN 37831, USA*
[c]*Computational Sciences and Engineering Division, Oak Ridge National Laboratory, Oak Ridge, TN 37831, USA*
[d]*Physical Sciences Division, Pacific Northwest National Laboratory, Richland, WA, 99354, USA*
[e]*Department of Materials Science and Engineering, University of Tennessee, Knoxville, TN 37996, USA. E-mail: wjweber@utk.edu*
[f]*Energy and Environment Science & Technology, Idaho National Laboratory, Idaho Falls, ID 83415, USA*
[g]*GSI Helmholtzzentrum, Darmstadt, 64291, Germany*
[h]*Technische Universität Darmstadt, 64287 Darmstadt, Germany*
[i]*University of Petroleum and Energy Studies, Dehradun 248007, India*

also been revealed in several pyrochlore structure oxides with various combinations of A-site (Gd, Sm, Yb, Hf, Er) and B-site (Ti, Zr, Sn) cations.[6–10] Under the irradiation of 2.8 MeV Au ion, a percolation of the disordered crystalline phase at the interface of $LaMnO_3$ and $SrTiO_3$ is observed.[11] All these findings highlight the importance of a detailed understanding of atomic arrangement to determine the phase transformation mechanisms resulting from ion-irradiation events, which is the focus of the present work. Our interest and focus of the present work is the development of an atomic-level understanding of the structural transformation induced by individual swift heavy ions (energy larger than 50 MeV) in $SrTiO_3$ that is a well-known wide-bandgap material and described as a critical foundational material in the area of functional oxide electronics.[12]

In $SrTiO_3$, defect evolution allows defect-driven non-stoichiometry to enable interesting electronic, magnetic, and optical properties.[12–14] For irradiations with low energy ions, Reagor *et al.* has reported that a partial alignment of TiO_6 octahedra occurs at the amorphous-crystalline interface formed in $SrTiO_3$ as a result of 300 eV Ar^+ irradiation, which leads to transformation from a highly non-conducting state to a metallic-equivalent conductive surface.[15] Ion irradiation of $SrTiO_3$ with Pt ions in the energy range of 0.1–1.0 MeV results in a crystalline-to-amorphous phase transformation at the surface of ~100 nm depth, which can be controlled *via* thermally-activated defect recovery stages.[16,17] Similarly, the damage accumulation in $SrTiO_3$ irradiated with 1.0 MeV Au ions causes amorphization, where similar disordering behavior is observed for both Sr and Ti sublattices.[18] Interestingly, during transmission electron microscopic investigations, the electron-beam-enhanced recrystallization of the amorphized phase is observed in irradiated $SrTiO_3$. Also, other amorphized oxide structures such as $Yb_2Ti_2O_7$ and apatites[19–21] show recrystallization under the electron beam, which is attributed to the local heating caused by electron excitation processes and energy transfer from energetic electrons to the lattice atoms.[22] When exposed to swift heavy ions in the MeV–GeV regime, each projectile produces along its trajectory a track, an amorphous cylindrical damage zone. Track formation requires that a critical electronic energy loss threshold of the ions is surpassed. Below this threshold, the track consists of a discontinuous string of damage clusters. The threshold was shown to be influenced by the synergetic effects of the nuclear and electronic energy-loss.[23] Pre-existing point defects formed by elastic collisions obviously facilitate the formation of amorphous tracks. Contrary to reports mentioned earlier, the tracks produced in the pre-damaged $SrTiO_3$ are stale under the electron beam without shrinking of the track diameter.[23] Similar observations of a stable amorphous phase under an electron beam were seen in laser-irradiated $SrTiO_3$,[24] which are attributed to insufficient energy deposition for the defect recovery process. Although these reports show a detailed understanding of ion-irradiation-induced amorphization and electron-beam-induced recrystallization, the present work identifies the significant gap in the atomic-level knowledge of the phase transition in $SrTiO_3$.

In our study, we create amorphous tracks in single crystalline $SrTiO_3$ by using swift heavy ions (629 MeV Xe) in the electronic energy loss regime. Sub-nanometer-level investigations of the atomic arrangement and lattice distortions are investigated by atomic-resolution imaging by means of scanning transmission electron microscopy (STEM) and data-driven image analysis. We further study the effect of electron-beam exposure on the formed ion tracks and investigate the characteristics of recrystallization *via in situ* observations. Molecular dynamics (MD) simulations shed additional light on the atomic order and possible cause of track recrystallization.

Methodology

Ion irradiation

Commercially available single crystalline $SrTiO_3$ was irradiated by 629 MeV Xe ions at the UNILAC linear accelerator of the GSI Helmholtz Center for Heavy Ion Research in Darmstadt. The applied fluence was 1×10^{11} ions per cm^2, which provided isolated tracks almost without track overlapping effects.

STEM characterization

The imaging was carried out on various samples in a fifth-order aberration-corrected scanning transmission electron microscope (Nion UltraSTEM200) operating at 200 keV. High-angle annular dark field (HAADF) imaging was done at an inner semi-angle of 65 mrad. We noticed a considerable strain contrast in the disordered region. Hence, the images will be referred to as annular dark field (ADF) throughout the investigation. The electron probe current used in the experiment is 28 ± 2 pA. The plan-view and cross-sectional samples for STEM studies are prepared using conventional mechanical polishing and thinning up to ~10 μm in an Allied Multiprep polisher. Subsequently, ion milling was carried out in Gatan PIPS-II ion mill to make them electron-transparent for STEM studies. Plan-view samples for STEM studies are prepared at a depth of ~5 μm from the irradiated surface where electronic energy-loss was almost constant at 28 keV nm^{-1} according to the Stopping and Range of Ions in Matter (SRIM) simulation. These samples were thinned only from the back side, followed by ion-milling with ion guns on both the sample sides.[25,26]

STEM image data analysis

In this work, the atomic-resolution ADF images are analyzed by extracting and separating the intensities of atomic columns of Sr and Ti and background. In the ADF images obtained in [001] zone axis, atomic columns contain exclusively Sr or Ti atoms and can be distinguished by their intensity, as shown in Fig. 1. This identification of cations generates the information on atomic-column coordinates and are mapped in terms of the localized strain, which is relevant to understanding cation ordering/disordering. The background intensity between the cationic atomic columns consists of background noise from the detector, and the intensity variations appear due to the strain contrast of O anions. The mapping of this background

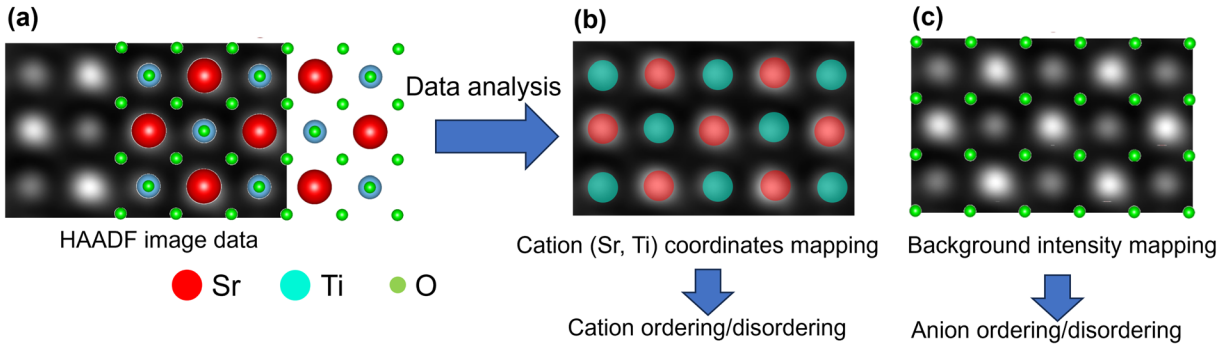

Fig. 1 (a) Atomic resolution ADF image with overlaying $SrTiO_3$ atomic model in [001] surface normal direction consisting of Sr (red), Ti (cyan), O (green) circles, (b) atomic columns of cations (Sr, Ti) extracted from intensity analysis of (a) yielding information on cation disordering, (c) map of extracted background intensity representing anionic (O) disordering.

intensity provides qualitative information on the ordering/disordering of oxygen column positions that can vary due to octahedral tilting or irradiation-induced distortions.

The identification of atomic columns in the atomic-resolution ADF images was performed using deep convolutional neural networks (DCNNs) where DCNN is trained with either Tensor Processing Unit (TPUv2) or with Tesla K80 Graphical Processing Unit (GPU) in Google Collaboratory with Tensorflow and Keras deep learning libraries and subsequently applied to analyze the acquired imaging data. Positions/coordinates of atoms (Sr and Ti) in ADF images were identified using AtomAI: Open-source software (**https://github.com/pycroscopy/atomai**), a Python library based on the Pytorch deep learning frameworks.[27,28] In this framework, the positions of Sr and Ti atomic columns are identified using the mean prediction model[27,28] that helps ascertain the atomic displacements, lattice distortions and localized strain at the atomic level. Fig. 2 shows a representative analysis of Sr and Ti identification (Sr: red and Ti: cyan) and the uncertainty in the feature recognition. The uncertainty in the atomic column recognition increases with the increase in the disordered region towards the amorphous phase. Thus, atoms cannot be recognized in the amorphous phase due to the lack of any specific feature (black track core of middle image). In the shell region, around the amorphous core, though the uncertainty is higher than the pristine $SrTiO_3$ lattice regions, it is sufficient to recognize the positions of the atoms accurately as shown in Fig. 2 (middle image).

Molecular dynamic simulations

The electronic energy-loss (S_e) and dpa profiles in $SrTiO_3$ induced by 629 MeV Xe irradiation were determined through the stopping and range of ions in matter (SRIM) code-2016.[29] The energy deposition from the hot electrons to the lattice atoms were numerically calculated by using the inelastic thermal spike (iTS) model.[30,31] Then, the calculated energy dissipation profiles were incorporated as input for MD simulations, which were performed using the DL_POLY code.[32] The DL_POLY code was used for the MD simulations, using the McCoy *et al.* potential, joined with the short-range ZBL poten-

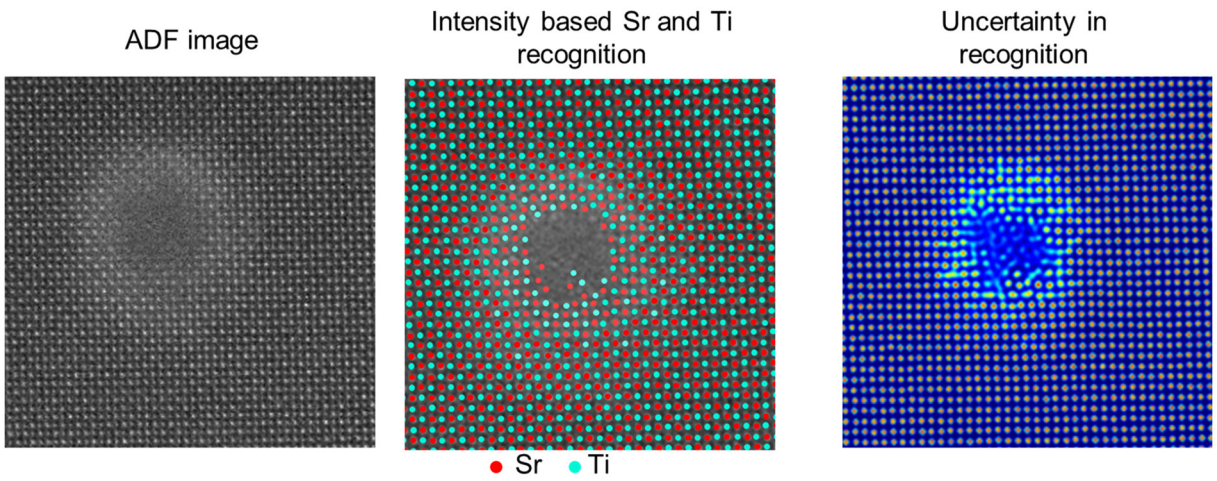

Fig. 2 ADF image of the sample region containing an individual amorphous ion-track in $SrTiO_3$. Image analysis yields identification of Sr (red) and Ti (cyan) atoms (middle image) and recognition uncertainty in the atomic features.

tial.[47] Equilibration of the systems was performed at 300 K under the constant-pressure and temperature (NPT) ensemble with 1 fs timestep. The irradiation simulations were performed under the constant-energy, constant-volume (NVE) ensemble using a variable timestep at 300 K. In the iTS calculations, the electron–phonon mean free path λ is equal to 4.7 nm, the electronic specific heat Ce is 1.0 J cm^{-3} K^{-1} and the diffusivity De is equal to 2 cm^2 s^{-1}. The details of the iTS model calculations and the MD simulations of the ion irradiations can be found the earlier published work.[33] To simulate the annealing due to the local melting that results in the interaction of $SrTiO_3$ with the electron beam, we annealed the systems at 5000 K for about 4 ns.

Results and discussion

The irradiated $SrTiO_3$ sample is analyzed at a near-surface having a penetration depth of 5 μm. The penetration depth to analyze the ion-tracks is determined using SRIM calculations for 629 MeV Xe ion. As shown in Fig. 3(a), the electronic energy-loss of the Xe ions remain constant at ~28.5 keV nm^{-1} until the depth of ~10 μm in $SrTiO_3$ and hereafter decreases to almost zero at a depth of ~28 μm. Meanwhile, nuclear energy loss remains negligible throughout this range except in the end-of-range regions, which is consistent with previous studies on various oxide systems.[6,10,25,34,35] These calculations provide a guideline to select the penetration depth for atomic-scale STEM investigations where the structural transformations are dominated by electronic energy-loss on incident ions in the lattice without nuclear interaction influence. It is assumed that ion-tracks would occur due to the local thermal spike during electronic energy-loss in low-conductive $SrTiO_3$. In the present case, ion irradiation effects are analyzed at a depth of 5 μm from the irradiation surface and the formation of ion-tracks is presented in Fig. 3(b–e). Fig. 3(b and c) shows plan-view ADF images of the formed ion-tracks in a [001] zone axis of $SrTiO_3$. The average size of the ion-tracks is estimated to be 8.5 ± 1 nm after swift Xe ion irradiation. Furthermore, Fig. 3(d and e) shows the bright field cross-sectional images at different magnifications, illustrating the formation of ion-tracks with diameter consistent with the plan-view images. The discontinuity in the ion-tracks can be interpreted based on the energy deposition in SrTiO3 lattice close to energy threshold for disordering, leading to partial melting of the lattice along the track length. Usually, this phenomenon is

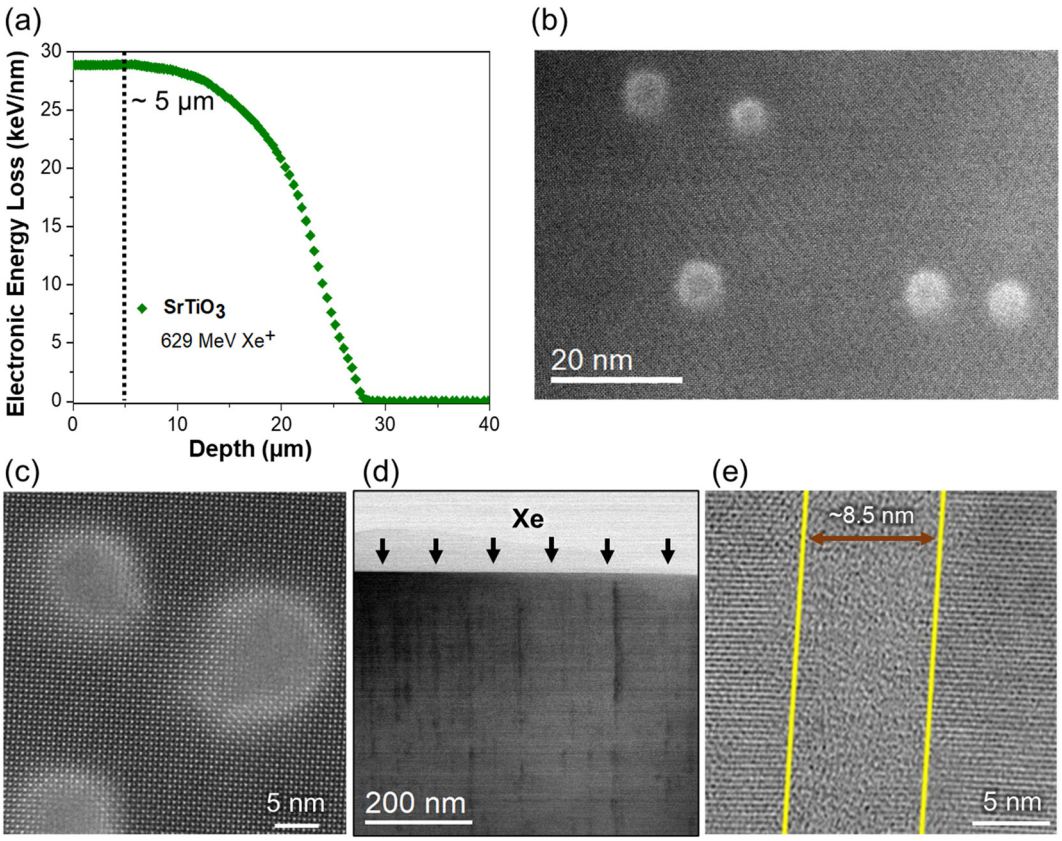

Fig. 3 (a) Electronic energy loss as a function of penetration depth in $SrTiO_3$ after 629 MeV Xe ion irradiation. (b) Plan-view ADF image revealing core–shell ion track formation (acquired at the depth of ~5 μm). (c) Atomic resolution ADF image of three ion-tracks revealing the formation of a core–shell track structure. (d) Cross-sectional annular bright-field (ABF) image of parallel oriented ion tracks embedded in $SrTiO_3$. (e) Cross-sectional ABF image illustrating the amorphous structure of an individual cylindrical track.

seen at relatively lower electronic energy-loss in materials but the efficacy of defect recombination due to energy dissipation and defect diffusion increases the threshold to higher energies in $SrTiO_3$. Similar observation of seeing discontinuous tracks has also been reported earlier formed by swift heavy ions in $SrTiO_3$.[36,37] It is also evident from the atomic-resolution images of the formed ion-tracks that an amorphous core (6.5 ± 1 nm) is surrounded by a brighter crystalline peripheral region (2 ± 0.5 nm). These regions can be distinguished based on the difference in contrast that is more prominent in the disordered area where the intensity in the ADF imaging is more sensitive to the strain fields evolving from irradiation-induced atomic disorder and defect formation along with the atomic number.[1]

For a more detailed analysis, we acquired several atomic-resolution ADF images (Fig. 4a) of ion-tracks and determined the atomic column coordinates of Sr and Ti cations based on their intensities. The dotted circles in the figure outline the presence of hallow region corresponding to background intensity. In the mapping of cation atomic columns (Fig. 4(b)) in [001] zone axis, Sr (red) and Ti (cyan) columns are identified based on their intensities that predominantly dependent on *Z*-contrast.[38] Based on the coordinates of Sr and Ti atoms, a cation strain map is deduced (Fig. 4(c)) on the region containing an ion track. The strain ($=\Delta d/d_{Sr-Ti}$) is calculated by estimating the atomic displacement (Δd) of Sr or Ti atoms from their ideal position and normalized with respect to the ideal *d*-spacing (d_{Sr-Ti}) of Sr–Ti in [001] zone axis. The results show that the strain in the unirradiated regions of $SrTiO_3$ lattice is almost negligible and increases in the disordered shell region around the amorphous track in the 4–6% range while maximizing at the crystalline-amorphous interface. Furthermore, the background intensity of the ADF images is also extracted, as shown in Fig. 4(d). The background intensity map reveals the results observed in the ADF images having brighter disordered crystalline shell region of the ion-tracks due to localized strain contrast emerging from O anion disordering.

The disordered crystalline structure created during track formation is attributed to TiO_6 octahedral distortions and/or the formation of highly distorted TiO_{6-x} polyhedral during extremely rapid melting and solidification. A similar phenomenon has also been seen in various pyrochlore-structured titanates and zirconates ($A_2B_2O_7$, A = Gd, Yb, Sm, Y, Nd, B = Ti, Zr or both)[9,35,39,40] where the peripheral shell structure transforms to a metastable defect fluorite phase instead of pyrochlore from melt phase during the recrystallization process.[6,26,41]

While investigating the ion-track atomic arrangement in STEM in $SrTiO_3$, it was noticed that the amorphous ion-tracks readily recrystallize under electron-beam irradiation. Fig. 5 shows various examples of *in situ* observations of e-beam-induced recrystallization of ion-tracks/amorphous regions. While the ion-track shown in Fig. 5(a) is the typical morphology seen as a result of swift heavy ion irradiation in $SrTiO_3$, other cases, although less often, are also observed in the sample. The ADF images (512 pixel × 512 pixel) were acquired with 5 μs per pixel of electron beam irradiation time on the samples, which is a sufficiently fast scan rate to capture this phenomenon in the microscope. Fig. 5 shows the first and 10^{th} frames from the continuously acquired image frames of the ion-tracks. As shown, different regions containing amorphous ion-tracks created by the impact of (a) single, (b) two, or (c) multiple ions in the vicinity recrystallize under e-beam irradiation. In a key observation from Fig. 5a and b, it has been seen that cationic reordering occurs remarkably well. However, it still shows significantly high background intensity due to strain contrast, signifying the presence of oxygen disordering. Fig. 5(d) shows a single ion stochastically creating a smaller amorphous region and it also gets recrystallized under e^- beam exposure. These above results reveal multiple evidence for the fact that ion-irradiated $SrTiO_3$ recrystallizes irrespective of different ion track scenarios like single, two, multiple and smaller ion-tracks.

A detailed study of the e-beam-induced recrystallization of one of the ion-tracks is presented in Fig. 6 using a frame-by-frame image analysis. The demonstrated ion-track consists of an amorphous core and a disordered peripheral region. The dotted circles in the images depict the amorphous and disordered regions originally present in the ion track (frame 0) for comparison with the subsequent recrystallization occurring during e^- beam irradiation. The results are shown of the initial amorphous core–shell ion-track (Frame 0) transforming to first partially recrystallized (Frame 10) and eventually fully

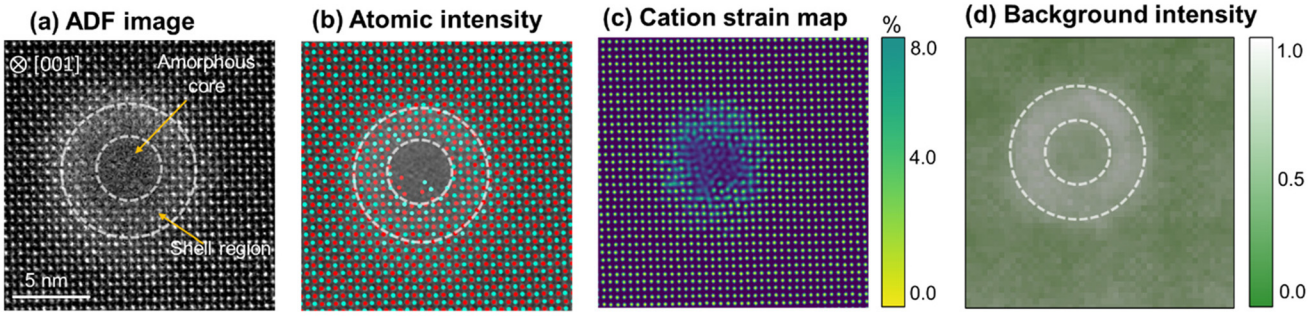

Fig. 4 (a) Atomic-resolution ADF image of a single core–shell ion track. (b) Atomic intensity map from (a) to identify the respective Sr (red) and Ti (cyan) positions. (c) Cation strain map obtained from coordinates deduced from (b). (d) Corresponding background intensity map. The dotted circles depict the original ion track in the frame 0 corresponding to background intensity.

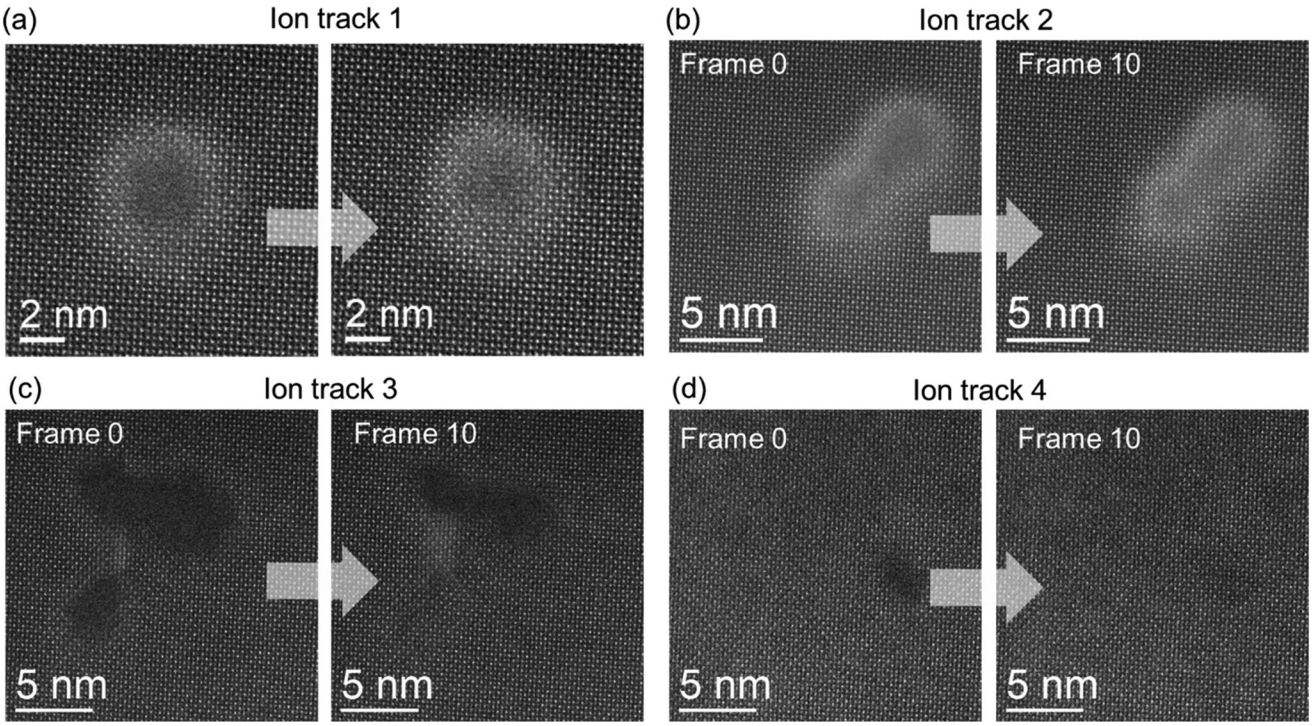

Fig. 5 Examples of *in situ* electron-beam recrystallization of amorphous ion-tracks after scanning and acquiring 10 frames of images. The regions represent ion-tracks formed by (a) a single ion, (b) two ions, (c) multiple ions in the vicinity and (d) a single ion stochastically creating a smaller amorphous region.

recrystallized ion track (Frame 20), respectively. Here, the positions of Sr and Ti atomic columns are determined for each acquired image (Fig. 6(a)) frame during electron irradiation based on the intensity of atomic columns (Fig. 6(b)). It has been seen that the intensity of Sr and Ti atoms in the recrystallizing regions are almost similar to that in the unirradiated matrix. However, while determining the strain between the atoms based on the obtained coordinates of atomic columns, the cationic strain has been observed to relax with the recrystallization process. As shown in Fig. 6(c), the strain is reduced from a maximum of ~8% in the initial stage core–shell structure to ~4% during partial recrystallization and ~2% in the fully recrystallized ion-track. This strain relaxation can be attributed to local annealing of the structure, which likes to return to the closest possible thermodynamically stable form during electron-beam irradiation. It is also important to note that the recrystallization process starts at the interface between the ordered and disordered region of the ion-track and propagates radially inwards. The pre-existing disorder, which anneals to attain a relatively more relaxed structure, acts as a template for amorphous phase recrystallization. Unlike ion-beam-induced epitaxial crystallization[16,42] which requires elevated temperatures and sufficient elastic energy transfers to cause significant displacement of atoms, this electron-beam-induced crystallization process occurs at room temperature and at energies insufficient to displace atoms. In another key observation based on the mapping of background intensity of ADF images as shown in Fig. 6(d), strain contrast remains present during the electron-beam irradiation even in a fully recrystallized stage. The background intensity is relatively higher in the pre-existing disordered zone and minimally reduced during recrystallization. This result can be attributed to significant oxygen vacancies in the pre-existing disordered zone that could not be healed during the recrystallization process. On the other hand, the initially existing amorphous phase in the ion-tracks consists of, although in short-range ordered form, significantly higher amounts of oxygen atoms and interstitials. Since the solidification rate during the original ion-track formation by energetic heavy ions occurs in much faster timescales of picoseconds-to-nanoseconds, trapping oxygen atoms is more likely. A similar phenomenon has been seen in other materials systems, such as in the formed ion-tracks in $Gd_2Ti_2O_7$ where pyrochlore structured, ordered region, disordered defect-fluorite region and amorphous region consisted of same composition within measurable limits.[9]

Fig. 7 illustrates the radially inwards recrystallization of the amorphous phase of the ion-track under e-beam irradiation at 200 keV. The circles in the images (from frame 0 to frame 20) represent the progressively decreasing size of the amorphous region with irradiation which ultimately disappears. This transformation begins epitaxially from a pre-existing crystalline matrix or the disordered crystalline region, which acts as a template for the amorphous region.[34] The HAADF images for this observation are taken with a pixel time of 5 μs per pixel.

Based on the acquired image frames (frame 0–20) of the ion-track, the positions of Sr and Ti atomic columns are deter-

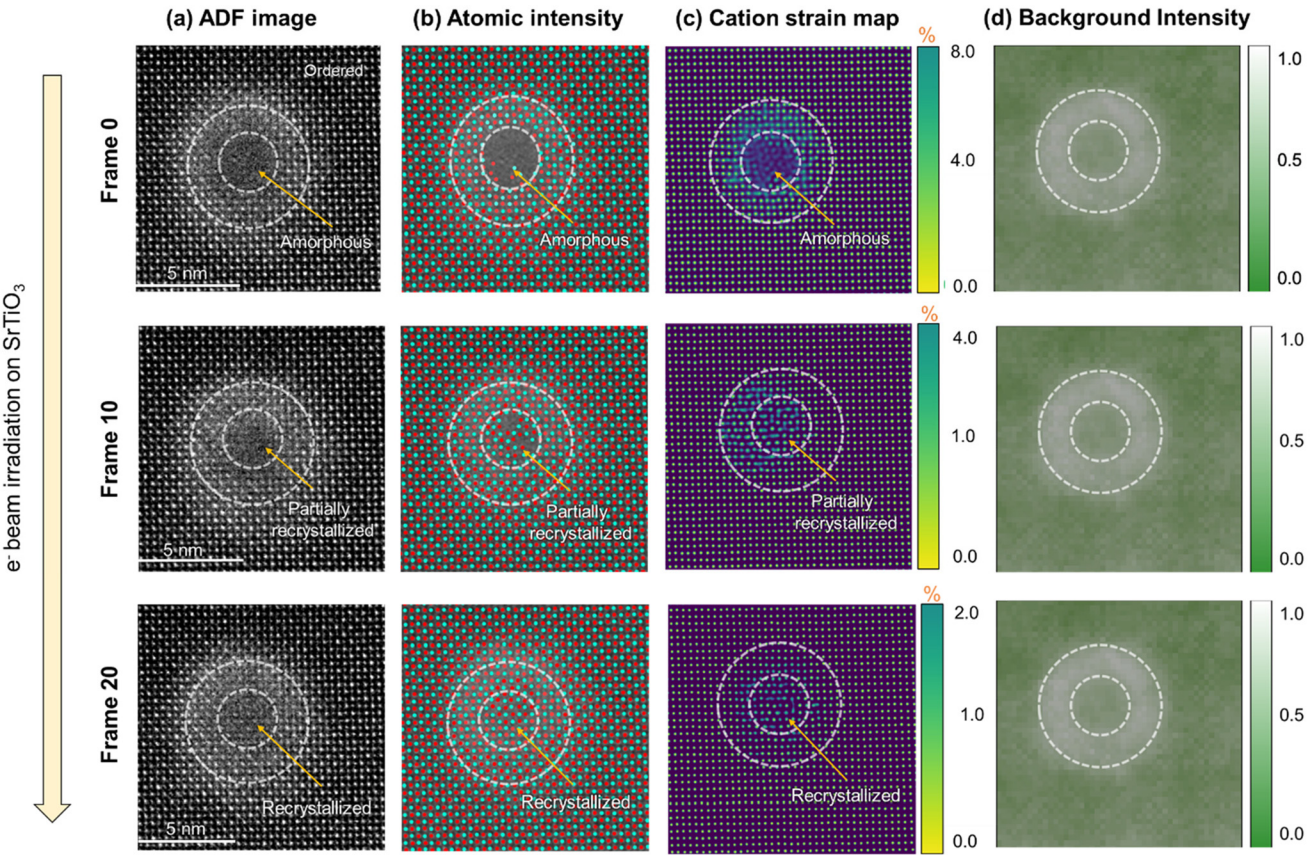

Fig. 6 (a) ADF images showing amorphous ion-track recrystallization progression in Frame (image) 0, 10 and 20 out of a total of 20 frames acquired of the ion-track. The recrystallization process was completed within 20 frames. (b) Atomic intensity map from the corresponding ADF image to identify the Sr and Ti positions, indicated by red and cyan colors, respectively. (c) Cation strain map obtained from coordinates determined in Figures shown in (b). (d) Background intensity maps corresponding to ADF images acquired with e^- beam irradiation. The dotted circles in all the images represent the amorphous and disordered regions of the original ion track as observed in frame 0. These circles can be seen as guidelines to observe the changes in recrystallized regions (both in cationic strain and background intensity representing anion strain) after e^- beam irradiation with respect to the Frame 0.

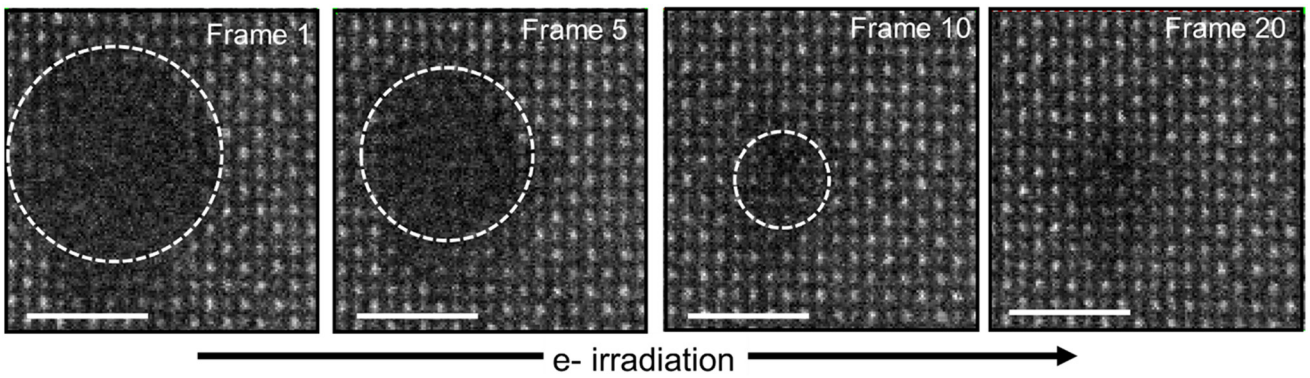

Fig. 7 HAADF images showing the radially inwards recrystallization of amorphous ion-tracks in SrTiO3 with subsequent e-beam irradiation. The circles in each image represent the decreasing amorphous regions of the ion-track. The scalebar shown in each image is of 2 nm.

mined to accurately estimate the change in amorphous region with respect to the original dimensions of the amorphous ion-track (frame 0). This variation of amorphous phase indicates that the rate of recrystallization is faster initially and retards in the later stages as shown in Fig. 8. The strain relaxation at the amorphous/crystalline interface of the ion-tracks can explain this observation. During the initial recrystallization, the strain accumulated was observed higher, easing the recrystallization

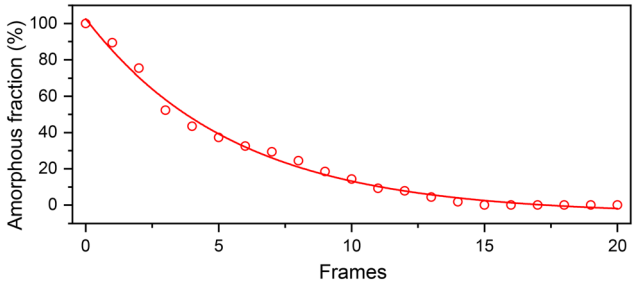

Fig. 8 Variation of the amorphous phase as a function of acquired frames during the process of electron beam recrystallization. The positions of Sr and Ti atomic columns are determined for each frame (*i.e* frame 0–frame 20) to estimate the variation of amorphous phase with acquired frames revealing faster recrystallisation in early stages which slowed down in the later frames.

process. During the recrystallization progression, a change in the present strain affects the rate of recrystallization, and the energy accumulated by electron-beam irradiation results in local heating that anneals the structure in the later stages.

The e^- beam-induced recrystallization process occurs at room temperature and with considerably less energy required to rearrange atoms than ion-beam-induced crystallization.[16] Electron beam-induced crystallization is attributed to the wide range of mechanisms, including enhanced defect mobility as a result of elastic (nuclear energy loss) and inelastic (electronic energy loss) energy transfer,[34] ionization process involving the breaking or rearrangement of unstable bonds,[43] and beam heating.[44] It is reported that the activation energy required for ion beam-induced recrystallization of $SrTiO_3$ is ~0.1–0.3 eV.[16,19] Electronic energy loss of 28.5 keV nm^{-1} in $SrTiO_3$ by swift heavy ions can transfer sufficient inelastic energy to target electrons, resulting in the local excitation of atoms that lead to atomic bond and structure rearrangement. This local excitation of atoms is effective in lowering the defect migration and recovery process and helping in vacancy-interstitial recombinations.[18] The electron irradiation energy is sufficient for multiple rearrangements of dangling-bond pairs that are thermodynamically less stable cation–oxygen bonds present in an amorphous matrix.[45] During the electron beam-induced recrystallization, it is also understood that the defect migration of these ionized atomic species takes place *via* local atomic hopping and atomic rearrangements leading to rotation of atomic polyhedra at the amorphous-crystalline interface. Previously, electron-beam-induced recrystallization has been reported in amorphous oxide systems, including $SrTiO_3$, $LaPO_4$, $ScPO_4$, and $ZrSiO_4$, in addition to other pyrochlore structure titanates.[18,19,45,46] One of the considerations in drawing in the feasibility of recrystallization of amorphous

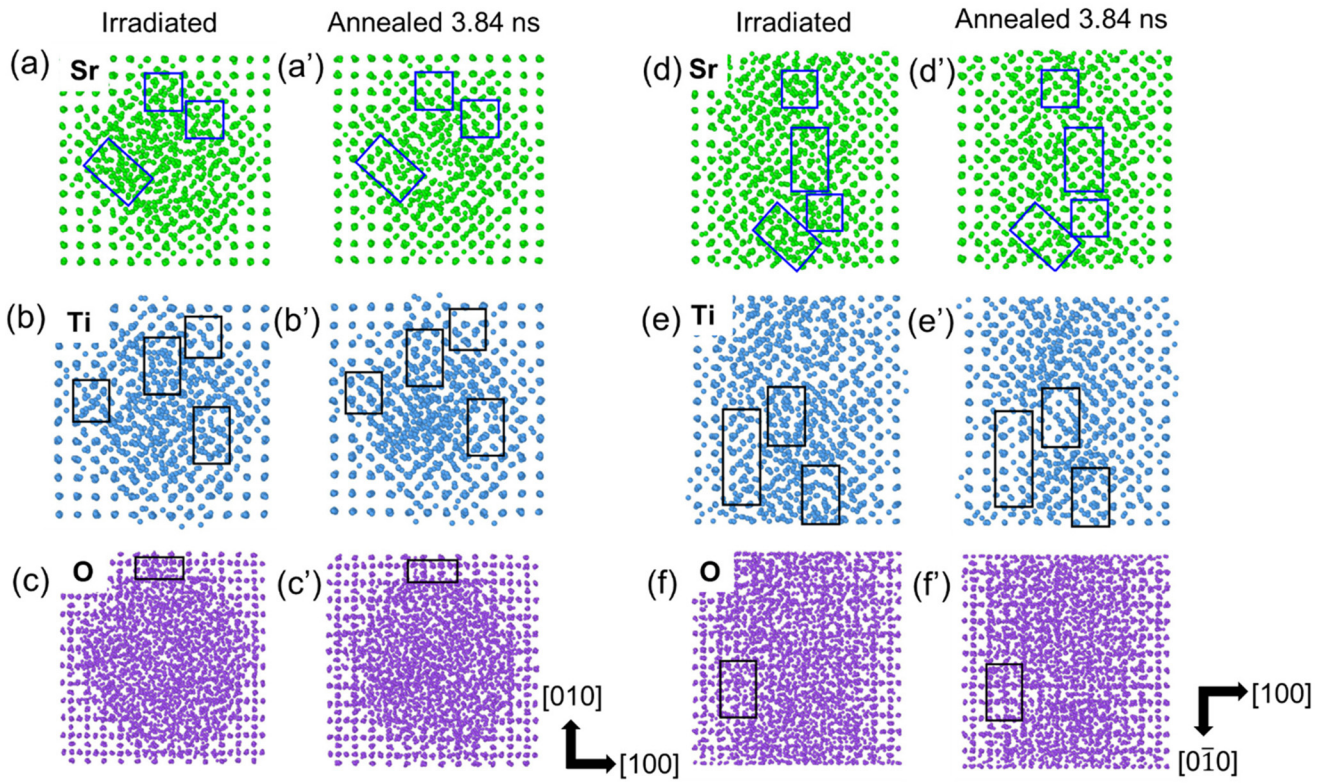

Fig. 9 MD-simulated ion track formation after 629 MeV Xe irradiation and its annealed structure after annealing at 5000 K. The MD-simulated results are captured for Sr, Ti, and, O atoms, respectively. The arrangement of Sr, Ti, and O atoms after Xe irradiation and annealed structure is captured: (a–c) plan view of MD-simulated structure, and (d–f) cross-sectional view of MD-simulated structure. The corresponding annealed structures are shown in (a'–f').

phases is the difference in the ionic radii of cations present in the A-site and B-site of the lattice. In the cases of pyrochlore titanates ($A_2Ti_2O_7$) with A-site consisting of Sm, Gd and Yb, it has been observed that as the A-site atoms are substituted from a larger size Sm to a smaller size Yb, the electron-beam recrystallization becomes feasible.[10] In addition, a similar effect was seen when smaller Ti atoms are replaced with larger Zr atoms to reduce the difference between A-site and B-site cationic radii. In the other cases of $LaPO_4$, $ScPO_4$, and $ZrSiO_4$, the same phenomenon has been observed where the relative difference of A-site and B-site ionic radii played the decisive role, and a three times higher dose of electrons was needed in $LaPO_4$ compared to $ScPO_4$, and $ZrSiO_4$. Although $SrTiO_3$ consists of a perovskite crystal structure, a similar rationale can be used to explain the recrystallization under an electron beam. In comparison to the difference in the ionic radii of the mentioned oxide systems (*e.g.* Gd/Ti, Yb/Ti, Sm/Ti *etc.*), the difference is lesser in the case between Sr and Ti, which favors faster atomic diffusion and lower energy barrier towards recrystallization.

Atomistic MD simulations were performed on $SrTiO_3$ to understand the recrystallization process, as shown in Fig. 9. An amorphous ion-track is first created in $SrTiO_3$ lattice by introducing a thermal spike profile that is calculated from the iTS model for electronic energy loss corresponding to 629 MeV Xe ions.[33] This thermal spike leads to local melting, quenching and restructuring over tens to hundreds of picoseconds. Fig. 9 shows the sublattices of Sr, Ti and O of the simulated ion-track in plan-view (a–c) and cross-sectional view (d–f) before and after annealing at 5000 K. In the simulated ion-track (irradiated), we do not see a disordered crystalline region as a continuous shell but just the sporadic disordered regions around the amorphous core. For better visualization, we have shown the parts of the shell regions containing the disordered crystalline regions, which overlay with the boxes in the images. One of the possibilities could be the limitation of simulations in producing the disordered regions due to stochastic distribution and recombinations of defects leaving the monolayer thin or no disordered layer. Another possibility could be the complexity in visualizing them due to the stacking of atoms with different disorders in the out-of-plane direction of the image, which appears more disordered.[36] For clarity, an apparent atomic rearrangement is noticed during the annealing process as seen in the enclosed boxes in the figure. It can be seen that recrystallization is easier in the Sr and Ti sublattices, as compared to the O sublattice, leaving behind oxygen vacancies, partial recrystallization and shell-structure formation. These results are consistent with the experimental results showing core–shell structure formation in ion-tracks, which demonstrated the presence of oxygen vacancies after electron-beam-induced recrystallization.

Conclusions

The results of this study clearly demonstrate that the structure and recrystallization of ion tracks in $SrTiO_3$ is rather complex at an irradiation energy of 629 MeV resulting in core–shell ion track formation. The ion track morphologies have been investigated using atomic-resolution ADF imaging and computational script-based image processing, which revealed that tracks produced with 629 MeV Xe ions have a core–shell structure consisting of an amorphous core (diameter 6.5 ± 1 nm) surrounded by a disordered crystalline shell (thickness 2 ± 0.5 nm). Cation disordering is revealed by determining the bond lengths of Sr–Sr and Ti–Ti atoms with data-driven methodology yielding information of cationic and anionic strain within the track area. In the amorphous track core, the strain is up to ~8% at the core–shell interface. Tracks exposed to the electron beam of the transmission electron microscope undergo pronounced recrystallization. With increased exposure time, the amorphous core shrinks radially, and the strain relaxes to about 2%. Interestingly, the strain in the shell region does not relax completely even after extended electron beam exposure. MD simulations confirm that the Sr and Ti sublattices easily rearrange during annealing whereas recrystallization of the O sublattices is more difficult, leaving behind oxygen disorder including interstitials and vacancies. Overall, our results offer a critical understanding of the atomic track structure in $SrTiO_3$ and the contributions of the specific sublattices during annealing processes.

Author contributions

A.K.G. and R.S. collected and analyzed STEM results. A.K.G., J. A.H., M.Z., Y.Z., C.T., E.Z., W.J.W., and R.S. all contributed to writing the manuscript. R.S., Y.Z., and W.J.W. initiated and coordinated the research. C.T., Y.Z., and W.J.W. performed the ion-irradiations and A.K.G., R.S., and J.A.H. acquired the results from electron microscopy. S.V.K. has prototyped the original analysis workflows. M.Z. prepared the scripts to analyze microscopy data. E.Z. performed the theory calculations and simulations.

Data availability

The data underlying this study are available in the published article and its online ESI.

Conflicts of interest

The authors declare no competing financial interest.

Acknowledgements

RS acknowledges the support of faculty start-up funding at Oklahoma State University. The electron microscopic data acquisition in this research was conducted at the Center for Nanophase Materials Sciences at ORNL, which is a DOE Office of Science User Facility. EZ (theory and simulation work) was

supported by the Center for Nanophase Materials Sciences, (CNMS), which is a US Department of Energy, Office of Science User Facility at Oak Ridge National Laboratory. The results presented here are based on a UMAT experiment that was carried out on the UNILAC accelerator at the GSI Helmholtz Center for Heavy Ion Research, Darmstadt (Germany) in the frame of FAIR Phase-0. The contribution of WJW was supported by the National Science Foundation under Grant No. DMR-2104228. YZ was supported as part of the Laboratory Directed Research and Development Program at Idaho National Laboratory under the Department of Energy (DOE) Idaho Operations Office (an agency of the U.S. Government) Contract DE-AC07-05ID145142. SVK was supported by the US Department of Energy, Office of Science, Office of Basic Energy Sciences, as part of the Energy Frontier Research Centers program: CSSAS – The Center for the Science of Synthesis Across Scales – under Award Number DE-SC0019288.

References

1 D. Kan, T. Terashima, R. Kanda, A. Masuno, K. Tanaka, S. Chu, H. Kan, A. Ishizumi, Y. Kanemitsu, Y. Shimakawa and M. Takano, Blue-Light Emission at Room Temperature from Ar^{+}-Irradiated $SrTiO_3$, *Nat. Mater.*, 2005, **4**, 3–6, DOI: 10.1038/nmat1498.

2 T. F. Nova, A. S. Disa, M. Fechner and A. Cavalleri, Metastable Ferroelectricity in Optically Strained $SrTiO_3$, *Science*, 2019, **364**, 1075–1079, DOI: 10.1126/science.aaw4911.

3 J. Hanzig, B. Abendroth, F. Hanzig, H. Stöcker, R. Strohmeyer, D. C. Meyer, S. Lindner, M. Grobosch, M. Knupfer, C. Himcinschi, U. Mühle, F. Munnik, R. Strohmeyer, D. C. Meyer, S. Lindner, M. Grobosch, M. Knupfer, C. Himcinschi and U. Mu, Single Crystal Strontium Titanate Surface and Bulk Modifications Due to Vacuum Annealing, *J. Appl. Phys.*, 2011, 064107, DOI: 10.1063/1.3638692.

4 L. Cao, A. Herklotz, D. Rata, C. Yin, O. Petracic, U. Kentsch, M. Helm and S. Zhou, Metal–Insulator Transition via Ion Irradiation in Epitaxial $La_{0.7}Sr_{0.3}MnO_3$-δ Thin Films, *Phys. Status Solidi RRL*, 2021, **15**(11), 1–5, DOI: 10.1002/pssr.202100278.

5 M. Lang, J. Lian, J. Zhang, F. Zhang, W. J. Weber, C. Trautmann and R. C. Ewing, Single-Ion Tracks in $Gd_2Zr_{2-x}Ti_xO_7$ Pyrochlores Irradiated with Swift Heavy Ions, *Phys. Rev. B: Condens. Matter Mater. Phys.*, 2009, **79**(22), 1–9, DOI: 10.1103/PhysRevB.79.224105.

6 R. Sachan, Y. Zhang, X. Ou, C. Trautmann, M. F. Chisholm and W. J. Weber, New Insights on Ion Track Morphology in Pyrochlores by Aberration Corrected Scanning Transmission Electron Microscopy, *J. Mater. Res.*, 2017, 928–935, DOI: 10.1557/jmr.2016.418.

7 J. Shamblin, M. Feygenson, J. Neuefeind, C. L. Tracy, F. Zhang, S. Finkeldei, D. Bosbach, H. Zhou, R. C. Ewing and M. Lang, Probing Disorder in Isometric Pyrochlore and Related Complex Oxides, *Nat. Mater.*, 2016, **15**(5), 507–511, DOI: 10.1038/nmat4581.

8 D. S. Aidhy, R. Sachan, E. Zarkadoula, O. Pakarinen, M. F. Chisholm, Y. Zhang and W. J. Weber, Fast Ion Conductivity in Strained Defect-Fluorite Structure Created by Ion Tracks in $Gd_2Ti_2O_7$, *Sci. Rep.*, 2015, **5**, 16297, DOI: 10.1038/srep16297.

9 R. Sachan, V. R. Cooper, B. Liu, D. S. Aidhy, B. K. Voas, M. Lang, X. Ou, C. Trautmann, Y. Zhang, M. F. Chisholm and W. J. Weber, Forging Fast Ion Conducting Nanochannels with Swift Heavy Ions: The Correlated Role of Local Electronic and Atomic Structure, *J. Phys. Chem. C*, 2017, **121**, 975–981, DOI: 10.1021/acs.jpcc.6b12522.

10 R. Sachan, M. F. Chisholm, X. Ou, Y. Zhang and W. J. Weber, Energetic Ion Irradiation-Induced Disordered Nanochannels for Fast Ion Conduction, *JOM*, 2019, **71**(1), 103–108, DOI: 10.1007/s11837-018-3171-y.

11 B. E. Matthews, M. Sassi, C. Barr, C. Ophus, T. C. Kaspar, W. Jiang, K. Hattar and S. R. Spurgeon, Percolation of Ion-Irradiation-Induced Disorder in Complex Oxide Interfaces, *Nano Lett.*, 2021, **21**(12), 5353–5359, DOI: 10.1021/acs.nanolett.1c01651.

12 W. D. Rice, P. Ambwani, M. Bombeck, J. D. Thompson, G. Haugstad, C. Leighton and S. A. Crooker, Persistent Optically Induced Magnetism in Oxygen-Deficient Strontium Titanate, *Nat. Mater.*, 2014, **13**(5), 481–487, DOI: 10.1038/NMAT3914.

13 O. O. Brovko and E. Tosatti, Controlling the Magnetism of Oxygen Surface Vacancies in $SrTiO_3$ through Charging, *Phys. Rev. Materials*, 2017, **1**, 00444405, DOI: 10.1103/PhysRevMaterials.1.044405.

14 S. H. Cha and Y. H. Han, Effects of Oxygen Vacancies on Relaxation Behavior of Mg-Doped $BaTiO_3$, *Jpn. J. Appl. Phys.*, 2006, 8–12, DOI: 10.1143/JJAP.45.7797.

15 D. W. Reagor and V. Y. Butko, Highly Conductive Nanolayers on Strontium Titanate Produced by Preferential Ion-Beam Etching, *Nat. Mater.*, 2005, **4**, 593–596, DOI: 10.1038/nmat1402.

16 K. Oyoshi, S. Hishita and H. Haneda, Study of Ion Beam Induced Epitaxial Crystallization of $SrTiO_3$, *J. Appl. Phys.*, 2000, **87**, 1–8, DOI: 10.1063/1.372365.

17 W. J. Weber, S. Thevuthasan, R. E. Williford, A. Meldrum and L. A. Boatner, *Ion-Beam-Induced Defects and Defects Interactions in Perovskite-Structure Titanates, NATO Science Series*, Springer, 2000, vol. 77. DOI: 10.1007/978-94-011-4030-0_32.

18 Y. Zhang, J. Lian, C. M. Wang, W. Jiang, R. C. Ewing and W. J. Weber, Ion-Induced Damage Accumulation and Electron-Beam-Enhanced Recrystallization in $SrTiO_3$, *Phys. Rev. B: Condens. Matter Mater. Phys.*, 2005, **72**, 094112, DOI: 10.1103/PhysRevB.72.094112.

19 I. Bae, Y. Zhang, W. J. Weber, M. Higuchi, L. A. Giannuzzi, I. Bae, Y. Zhang and W. J. Weber, Electron-Beam Induced Recrystallization in Amorphous Apatite, *Appl. Phys. Lett.*, 2007, **90**, 021912, DOI: 10.1063/1.2430779.

20 I. Bae, Y. Zhang and W. J. Weber, Ionization-Induced Effects in Amorphous Apatite at Elevated Temperatures,

J. Mater. Res., 2008, **23**, 962–967, DOI: 10.1557/JMR.2008.0114.

21 I. Bae, Y. Zhang, W. J. Weber, M. Ishimaru, Y. Hirotsu and M. Higuchi, Temperature Dependence of Electron-Beam Induced Effects in Amorphous Apatite, *Nucl. Instrum. Methods Phys. Res., Sect. B*, 2008, **266**, 3037–3042, DOI: 10.1016/j.nimb.2008.03.160.

22 W. J. Weber, H. Xue, E. Zarkadoula and Y. Zhang, Two Regimes of Ionization-Induced Recovery in $SrTiO_3$ under Irradiation, *Scr. Mater.*, 2019, **173**, 154–157, DOI: 10.1016/j.scriptamat.2019.08.013.

23 W. J. Weber, E. Zarkadoula, O. H. Pakarinen, R. Sachan, M. F. Chisholm, P. Liu, H. Xue, K. Jin and Y. Zhang, Synergy of Elastic and Inelastic Energy Loss on Ion Track Formation in $SrTiO_3$, *Sci. Rep.*, 2015, **5**, 7726, DOI: 10.1038/srep07726.

24 A. K. Gupta, S. Gupta, S. Mandal and R. Sachan, Laser Irradiation-Induced Nanoscale Surface Transformations in Strontium Titanate, *Crystals*, 2022, **12**(624), 1–11, DOI: 10.3390/cryst12050624.

25 R. Sachan, O. H. Pakarinen, P. Liu, M. K. Patel, M. F. Chisholm, Y. Zhang, X. L. Wang and W. J. Weber, Structure and Band Gap Determination of Irradiation-Induced Amorphous Nano-Channels in $LiNbO_3$, *J. Appl. Phys.*, 2015, **117**, 135902, DOI: 10.1063/1.4915932.

26 R. Sachan, E. Zarkadoula, M. Lang, C. Trautmann, Y. Zhang, M. F. Chisholm and W. J. Weber, Insights on Dramatic Radial Fluctuations in Track Formation by Energetic Ions, *Sci. Rep.*, 2016, **6**, 27196, DOI: 10.1038/srep27196.

27 M. Ziatdinov and S. Kalinin, AtomAI : Open-Source Software for Applications of Deep Learning to Microscopy Data, *Microsc. Microanal.*, 2021, **27**(Suppl 1), 3000–3002, DOI: 10.1017/S1431927621010436.

28 M. Ziatdinov, Y. Liu, K. Kelley, R. Vasudevan and S. V. Kalinin, Bayesian Active Learning for Scanning Probe Microscopy: From Gaussian Processes to Hypothesis Learning, *ACS Nano*, 2022, **16**, 13492–13512, DOI: 10.1021/acsnano.2c05303.

29 J. F. Ziegler, M. D. Ziegler and J. P. Biersack, SRIM – The Stopping and Range of Ions in Matter (2010), *Nucl. Instrum. Methods Phys. Res., Sect. B*, 2010, **268**(11–12), 1818–1823, DOI: 10.1016/j.nimb.2010.02.091.

30 M. Toulemonde, Irradiation by Swift Heavy Ions : Influence of the Non-Equilibrium Projectile Charge State for near Surface Experiments, *Nucl. Instrum. Methods Phys. Res., Sect. B*, 2006, **250**, 263–268, DOI: 10.1016/j.nimb.2006.04.163.

31 H. Xue, E. Zarkadoula, P. Liu, K. Jin, Y. Zhang and W. J. Weber, Amorphization Due to Electronic Energy Deposition in Defective Strontium Titanate, *Acta Mater.*, 2017, **127**, 400–406, DOI: 10.1016/j.actamat.2017.01.051.

32 I. T. Todorov, W. Smith and M. T. Dove, *DL_POLY_3: New Dimensions in Molecular Dynamics Simulations via Massive Parallelism*, 2006. DOI: 10.1039/b517931a.

33 H. Xue, E. Zarkadoula, R. Sachan, Y. Zhang, C. Trautmann and W. J. Weber, Synergistically-Enhanced Ion Track Formation in Pre-Damaged Strontium Titanate by Energetic Heavy Ions, *Acta Mater.*, 2018, **150**, 351, DOI: 10.1016/j.actamat.2018.03.027.

34 R. Sachan, E. Zarkadoula, X. Ou, C. Trautmann, Y. Zhang, M. F. Chisholm and W. J. Weber, Sculpting Nanoscale Functional Channels in Complex Oxides Using Energetic Ions and Electrons, *ACS Appl. Mater. Interfaces*, 2018, **10**, 16731–16738, DOI: 10.1021/acsami.8b02326.

35 E. C. O'Quinn, C. L. Tracy, W. F. Cureton, R. Sachan, J. C. Neuefeind, C. Trautmann and M. K. Lang, Multi-Scale Investigation of Heterogeneous Swift Heavy Ion Tracks in Stannate Pyrochlore, *J. Mater. Chem. A*, 2021, **9**(31), 16982–16997, DOI: 10.1039/d1ta04924k.

36 X. Han, E. Zarkadoula, Q. Huang, M. L. Crespillo, X. Wang and P. Liu, Concentric core-shell tracks and spectroscopic properties of $SrTiO_3$ under intense electronic excitation, *Nano Today*, 2022, **46**, 101612, DOI: 10.1016/j.nantod.2022.101612, ISSN 1748-0132.

37 H. Xue, E. Zarkadoula, R. Sachan, Y. Zhang, C. Trautmann and W. J. Weber, Synergistically-enhanced ion track formation in pre-damaged strontium titanate by energetic heavy ions, *Acta Mater.*, 2018, **150**, 351–359, DOI: 10.1016/j.actamat.2018.03.027, ISSN 1359-6454.

38 S. J. Pennycook, Z-Contrast Transmission Electron Microscopy, *Annu. Rev. Mater. Sci.*, 1992, **22**, 171–195, DOI: 10.1146/annurev.ms.22.080192.001131va.

39 D. S. Aidhy, R. Sachan, E. Zarkadoula, O. Pakarinen, M. F. Chisholm, Y. Zhang and W. J. Weber, Fast Ion Conductivity in Strained Defect-Fluorite Structure Created by Ion Tracks in $Gd_2Ti_2O_7$, *Sci. Rep.*, 2015, **5**, 16297, DOI: 10.1038/srep16297.

40 R. Sachan, M. F. Chisholm, X. Ou, Y. Zhang and W. J. Weber, Energetic Ion Irradiation-Induced Disordered Nanochannels for Fast Ion Conduction, *JOM*, 2019, **71**(1), 103–108, DOI: 10.1007/s11837-018-3171-y.

41 J. Zhang, M. Lang, R. C. Ewing, R. Devanathan, W. J. Weber and M. Toulemonde, Nanoscale Phase Transitions under Extreme Conditions within an Ion Track, *J. Mater. Res.*, 2010, **25**(07), 1344–1351, DOI: 10.1557/JMR.2010.0180.

42 N. Jiang, Damage Mechanisms in Electron Microscopy of Insulating Materials, *J. Phys. D: Appl. Phys.*, 2013, **46**, 305502, DOI: 10.1088/0022-3727/46/30/305502.

43 I. Jenčič, M. W. Bench, I. M. Robertson and M. A. Kirk, Electron-Beam-Induced Crystallization of Isolated Amorphous Regions in Si, Ge, GaP and GaAs, *J. Appl. Phys.*, 1995, **78**, 974–982, DOI: 10.1063/1.360764.

44 W. J. Weber, J. W. Wald and H. Matzke, Effects of Self-Radiation Damage in Cm-Doped $Gd_2Ti_2O_7$ and $CaZrTi_2O_7$, *J. Nucl. Mater.*, 1986, **138**, 196–209, DOI: 10.1016/0022-3115(86)90006-1.

45 A. Meldrum, L. A. Boatner and R. C. Ewing, Electron-Irradiation-Induced Nucleation and Growth in Amorphous $LaPO_4$, $ScPO_4$, and Zircon, *J. Mater. Res.*, 1997, **12**, 1816–1827, DOI: 10.1557/JMR.1997.0250.

46 S. Jesse, Q. He, A. R. Lupini, D. N. Leonard, M. P. Oxley, O. Ovchinnikov, R. R. Unocic, A. Tselev, M. Fuentes-Cabrera, B. G. Sumpter, S. J. Pennycook, S. V. Kalinin and

A. Y. Borisevich, Atomic-Level Sculpting of Crystalline Oxides: Toward Bulk Nanofabrication with Single Atomic Plane Precision, *Small*, 2015, **11**, 5895–5900, DOI: **10.1002/smll.201502048**.

47 M. A. McCoy, R. W. Grimes and W. E. Lee, Phase stability and interfacial structures in the SrO–SrTiO3 system, *Philos. Mag. A*, 1997, **75**, 833–846, DOI: **10.1080/01418619708207205**.